

Bayesian predictions of reynolds-averaged navier–stokes uncertainties using maximum a posteriori estimates

Edeling, Wouter N.; Schmelzer, Martin; Dwight, Richard P.; Cinnella, Paola

DOI

[10.2514/1.J056287](https://doi.org/10.2514/1.J056287)

Publication date

2018

Document Version

Final published version

Published in

AIAA Journal

Citation (APA)

Edeling, W. N., Schmelzer, M., Dwight, R. P., & Cinnella, P. (2018). Bayesian predictions of reynolds-averaged navier–stokes uncertainties using maximum a posteriori estimates. *AIAA Journal*, *56*(5), 2018-2029. <https://doi.org/10.2514/1.J056287>

Important note

To cite this publication, please use the final published version (if applicable). Please check the document version above.

Copyright

Other than for strictly personal use, it is not permitted to download, forward or distribute the text or part of it, without the consent of the author(s) and/or copyright holder(s), unless the work is under an open content license such as Creative Commons.

Takedown policy

Please contact us and provide details if you believe this document breaches copyrights. We will remove access to the work immediately and investigate your claim.



Bayesian Predictions of Reynolds-Averaged Navier–Stokes Uncertainties Using Maximum a Posteriori Estimates

Wouter N. Edeling*

Stanford University, Stanford, California 94305

Martin Schmelzer[†] and Richard P. Dwight[‡]

Delft University of Technology, 2629 HS Delft, The Netherlands
and

Paola Cinnella[§]

Arts et Métiers ParisTech, 75013 Paris, France

DOI: 10.2514/1.J056287

Computational fluid dynamics analyses of high-Reynolds-number flows mostly rely on the Reynolds-averaged Navier–Stokes equations. The associated closure models are based on multiple simplifying assumptions and involve numerous empirical closure coefficients, which are calibrated on a set of simple reference flows. Predicting new flows using a single closure model with nominal values for the closure coefficients may lead to biased predictions. Bayesian model-scenario averaging is a statistical technique providing an optimal way to combine the predictions of several competing models calibrated on various sets of data (scenarios). The method allows a stochastic estimate of a quantity of interest in an unmeasured prediction scenario to be obtained by 1) propagating posterior probability distributions of the parameters obtained for multiple calibration scenarios, and 2) computing a weighted posterior predictive distribution. Although step 2 has a negligible computational cost, step 1 requires a large number of samples of the solver. To enable the application of the proposed approach to computationally expensive flow configurations, a modified formulation is used where a maximum posterior probability approximation is used to drastically reduce the computational burden. The predictive capability of the proposed simplified approach is assessed for two-dimensional separated and three-dimensional compressible flows.

I. Introduction

DIRECT numerical computation of turbulent flowfields is computationally intractable for most applications. Several levels of approximation are possible, according to flow scales that are resolved/modeled. In all cases, scale separation introduces unclosed terms that need to be modeled. The choice of the appropriate modeling level remains essentially a matter of expert judgment. In particular, it will always depend on cost versus accuracy considerations. On the other hand, even once a given level has been selected, the simplifying assumptions introduce unclosed terms for which several possible submodels may be designed. These may differ in both their mathematical structure and their closure parameters. The common practice in turbulence modeling is often to leave the choice of a specific model structure to expert judgment while treating model constants as adjustable parameters that are calibrated in such a way as to reproduce simple well-documented flows. Both of the preceding aspects, however, represent sources of uncertainty in the prediction of a new flow.

Although more general modeling approaches like large-eddy simulation have made considerable progress in the last decade, turbulence models based on Reynolds-averaged Navier–Stokes (RANS) will remain the workhorse tools for engineering design and optimization in the decade to come. An extremely large variety of RANS models has been proposed in the past, ranging from simple

algebraic models to sophisticated Reynolds stress models (see [1] for a review). However, in order to arrive at any given closure model, numerous assumptions in the mathematical derivation and subsequent calibration must be made. No universally accepted and valid model has been identified in computational fluid dynamics (CFD) literature, meaning that the appropriateness of a given model structure is highly uncertain when predicting a new configuration. Additionally, RANS models are developed and calibrated on simple flows using noisy experimental data, and they are applied to radically different flows with the same coefficients. Furthermore, because these calibrations are deterministic (and, as experimental uncertainty, are generally ignored), one obtains point estimates for the closure coefficients. This ultimately leads to predictions that are subject to unknown degrees of uncertainty, especially if the flow configuration of interest is far removed from the flow scenarios under which the model was calibrated.

The aforementioned uncertainties in RANS models can be addressed by means of statistical tools. All such tools are meant to quantify the uncertainty in RANS closures, and they should not be considered as a replacement for deterministic simulations. In the context of uncertainty quantification (UQ), uncertainties associated with the closure coefficients are referred to as parametric uncertainties. These can be effectively addressed by replacing standard deterministic calibration with statistical calibration, see, e.g., [2–4]. Specifically, Bayesian calibration allows one to infer posterior probability distributions of the closure parameters, given some available set of experimental data. However, it is important to stress that a posterior distribution might only display a predictive capability for the flow case for which it was calibrated. In [5], Edeling et al. performed multiple Bayesian calibrations for the coefficients of the well-known $k - \epsilon$ model [6] using experimental velocity data from boundary layers subject to a wide range of different pressure gradients. Even though the flow topology was the same for all calibration cases (i.e., boundary layers), the resulting posterior distributions were significantly different. This variability of posterior distributions is a measure for the lack of predictive capability of a given model due to the simplifying assumptions in its mathematical structure.

Received 5 June 2017; revision received 27 November 2017; accepted for publication 28 November 2017; published online 11 January 2018. Copyright © 2017 by W. N. Edeling. Published by the American Institute of Aeronautics and Astronautics, Inc., with permission. All requests for copying and permission to reprint should be submitted to CCC at www.copyright.com; employ the ISSN 0001-1452 (print) or 1533-385X (online) to initiate your request. See also AIAA Rights and Permissions www.aiaa.org/randp.

*Postdoctoral Research, Center for Turbulence Research, 488 Escondido Mall, 500A.

[†]Ph.D. Candidate, Faculty of Aerospace Engineering, Department of Aerodynamics, Kluyverweg 2.

[‡]Professor, Faculty of Aerospace Engineering, Department of Aerodynamics, Kluyverweg 2.

[§]Professor, Laboratoire DynFluid, 151 Boulevard de l'Hopital.

The model needs adjusted coefficients for each new case to counterbalance deficiencies inherent to neglecting part of the flow physics.

The second class of uncertainty (namely, model-form uncertainty) arises through the assumptions that are made in the mathematical form of the closure model. Many different models exist, and their performances are known to be flow dependent; see, e.g., [7,8]. Previous attempts to tackle model-form uncertainty include calibrations of a modified eddy viscosity field [9], the introduction of statistical error terms in the calibration procedure [2,10] or in the model transport equations [11], and the use of a stochastic counterpart of the Reynolds stress tensor [12]. Even UQ techniques for the RANS equations with no modeling, where the transport terms are represented with direct numerical simulation data, have been developed [13,14]. All these methods rely on detailed data from direct numerical simulations to infer about stochastic fields. Although promising, the aforementioned methodologies suffer from at least one of the following drawbacks:

1) Direct numerical simulation (DNS) data are available only for relatively simple low-Reynolds-number configurations.

2) Inferring the stochastic (eddy viscosity or error) fields involves costly optimization algorithms, e.g., to maximize the likelihood of observing the data.

3) Extrapolating the stochastic correction terms to the prediction of unseen configurations is still an open problem, especially for realistic flow configurations.

Other means for representing model-form uncertainty include the use of a multimodel framework. A relevant example can be found in the work of Poroseva et al. [15], where the Dempster–Shafer evidence theory was used to obtain a measure of the total uncertainty in the mean velocity predictions around a RAE 2822 airfoil. Dempster’s rule is used to fuse the predictions of two closure models and, using only sparse experimental data, the authors of [15] predicted the velocity with quantified uncertainty at locations in the same flow where no data were available. Multimodel approaches have also found application in meteorology [16,17], hydrology [18], and climate science [19], to name just a few.

We will focus on Bayesian model-scenario averaging (BMSA) [20], which provides a coherent framework to address both parametric and model-form uncertainties, providing a robust predictive method (see, for instance, [21] for an application to groundwater modeling uncertainties). Like Bayesian model averaging (BMA), BMSA combines the predictions from multiple models, thereby providing a measure for (closure) model uncertainty [22]. In addition, BMSA can combine the posterior distributions from different calibration scenarios, which allows one to compute error estimates due to scenario variability. Unless this variability is negligible, one should not assume that obtained parameter estimates are extrapolative to other flow scenarios. In other words: combining multiple nonoverlapping posteriors adds uncertainty to the assumption that a posterior distribution can be applied outside the flow scenario under which it was calibrated.

In this paper, we rely solely on RANS models for prediction. Hence, we cannot assume that the true model that generated the data is contained in our selected model set; although, in principle higher-fidelity models, could be included in the Bayesian average at increased computational cost. It should therefore be noted that subject-matter expertise, applied to the selection of competing models (and scenarios), is still important for maintaining predictive accuracy. As noted by Draper [20], although multimodel approaches still introduce a bias in the prediction, due to the selection of a finite set of model structures, they play a useful role in reducing the bias with respect to predictions based on a single model structure.

In previous work [23], BMSA was used to construct a stochastic model for predicting boundary-layer flows subject to an arbitrary pressure gradient, based on multiple RANS models calibrated using selected experimental boundary-layer data. Specifically, we applied BMSA using five closure models and 14 boundary-layer calibration scenarios (corresponding to various external pressure gradients) to predict unobserved boundary-layer flows subject to an arbitrary pressure gradient. Each individual calibration was performed using

the Bayesian method developed by the authors of [2,24]. Other notable means of stochastic parameter estimation can be found in [25,26]. Both the calibration and the prediction phases relied on a fast boundary-layer code. When addressing more complex, computationally intensive, flow configurations, a clear downside of BMSA is the associated computational burden. The first cost is associated to the calibration phase, in which the Markov-chain Monte Carlo method [27] is used to draw samples from the posterior distribution. Furthermore, the predictive phase of the BMSA procedure dictates the need to propagate $I \times K$ (with I being the number of competing models and K the number of calibration scenarios) posterior distributions through a RANS code applied to the flow scenario of interest, which is prohibitively expensive for most practical flow configurations. A common option is to replace the expensive RANS code with a much cheaper surrogate model such as, for instance, a polynomial approximation created with stochastic collocation or polynomial chaos methods [28]. Still, creating the surrogate model will require samples from the full RANS code, and surrogate modeling techniques are subject to the so-called curse of dimensionality. The number of required code samples therefore rises exponentially with the number of unknown parameters.

Our goal for this paper is to assess the predictive capability of the BMSA method for computationally expensive flow cases while using the most drastic cost reduction technique possible to speed up the prediction step. We assume that the calibration cost is less critical because it is done only once in a preliminary phase. Specifically, in this work, we use the posterior distributions of [23] and propagate them through new flow configurations described by a full RANS solver instead of a boundary-layer code. Note that posterior distributions resulting from additional calibration scenarios can be added as soon as they become available.

To drastically reduce the computational cost associated with the propagation step, we approximate each posterior as a Dirac delta distribution centered at the maximum a posteriori (MAP) estimate. Now, instead of having to propagate $I \times K$ posteriors, we are left with $I \times K$ deterministic evaluations. To evaluate the predictive capability of the proposed modified BMSA approach, we selected a number of flow problems that include physics that the boundary-layer trained BMSA model was not subjected to during the calibration phase.

This paper is organized as follows. First, we will give a very brief overview of the competing closure models considered in this paper. In Sec. III, we describe our reduced BMSA method using MAP estimates. Preliminary validations of the MAP-base BMSA approach are carried out in Sec. IV using the boundary-layer flow cases of [23]. Section V shows the results obtained for the different prediction flow cases. Finally, we give our conclusion in Sec. VI.

II. RANS Turbulence Models

In the present work, we restrict our attention to three transport equation models largely employed in engineering applications. These are selected from the family of so-called linear eddy viscosity models, which adopt a linear representation of the Reynolds stress tensor, based on the well-known Boussinesq assumption. We use the $k - \epsilon$, $k - \omega$, and Spalart–Allmaras (SA) models.

As these are very well-known models, we do not give full details for the sake of conciseness. Rather, we refer to [1] for a complete description of their mathematical structure. Also, all values for the closure coefficients (both nominal and perturbed) can be found in the Appendix.

III. Bayesian Predictive Methodology

We describe a statistical methodology based on Bayesian model-scenario averaging for making predictions of a chosen quantity of interest (QOI). BMSA provides a coherent framework for combining predictions from multiple competing conceptual models and calibration data to attain a more realistic and reliable description of the predictive uncertainty.

A. BMSA Formulation

Consider a particular flow of interest, including boundary conditions, material parameters, and all other physical properties needed to define it unambiguously. This we term a scenario, denoted S . Assume that there are reference data \mathbf{z} available for S , which may be measurements of any flow quantity or data from higher-fidelity simulations (e.g., DNS). Let $m_{\text{CFD}}(S; M, \theta)$ be a governing model, here represented by a CFD code, which takes as arguments the scenario S , a turbulence model M , and its closure coefficients θ . Note that the size of θ and the meaning of its components will depend on M . Let the model return the full state of the fluid in all variables. Then, we can define an operator $H_z(\cdot)$ that maps the state to the observed quantities \mathbf{z} (this can be, e.g., a procedure for extracting the aerodynamic coefficients from the full solution for the flow around a body or a velocity profile at a given station). The model output is then given by $H_z \circ m_{\text{CFD}}(S; M, \theta)$ and can be related to the observed data by means of a statistical model. One such model, used in [5,23], is represented by the following:

$$\mathbf{z} = \eta H_z \circ m_{\text{CFD}}(S; M, \theta) + \epsilon \quad (1)$$

where ϵ and η are random variables representing the measurement noise and model error, respectively. The latter accounts for the fact that, even with the best possible parameters, the model does not predict the true value for \mathbf{z} , due to errors intrinsic to modeling assumptions. The multiplicative model-error term of Eq. (1) was first introduced in [29]. Additive models are also available; see, e.g., [26]. We assume throughout that the CFD calculations have run on sufficiently fine grids, such that errors due to grid resolution are significantly less than the uncertainty due to modeling assumptions. We also assume that the calculations have well converged to the steady-state solution. The experimental noise term ϵ is modeled using a zero-mean Gaussian distribution.

The observations available for a given S can be used to infer the model parameters θ using a Bayesian calibration approach, i.e., by applying Bayes's rule:

$$p(\theta|\mathbf{z}, M, S) = \frac{p(\mathbf{z}|\theta, M, S)p(\theta|M, S)}{p(\mathbf{z}|M, S)} \quad (2)$$

where $p(\theta|\mathbf{z}, M, S)$ is the joint posterior probability distribution of the closure coefficients under the given turbulence model and the calibration data \mathbf{z} observed for scenario S . Furthermore, $p(\theta|M, S)$ is the joint prior probability distribution for the model coefficients, which summarizes available knowledge about θ before observing any data. The likelihood function $p(\mathbf{z}|\theta, M, S)$, which stems from the statistical model [Eq. (1)], describes the probability of observing the data for scenario S , given a model and a realization of the closure coefficients. Evaluating $p(\mathbf{z}|\theta, M, S)$ for a given realization of θ involves running m_{CFD} and is, as such, a costly operation. Finally, $p(\mathbf{z}|M, S)$ is the evidence of the data, which normalizes the posterior distribution. Because $p(\mathbf{z}|M, S)$ does not depend upon θ , it does not have to be computed while calibrating θ .

Given the complexity of the likelihood function, the posterior $p(\theta|\mathbf{z}, M, S)$ cannot be obtained analytically and is instead evaluated numerically. We employ the Markov-chain Monte Carlo method [27] to draw samples from Eq. (2). To reach convergence of the Markov chain, it was observed that $\mathcal{O}(10^4)$ code samples were required [5]. Ordinarily, this would constitute an excessive strain on available computational resources in a CFD context. In previous work [23], the experimental data consisted of boundary-layer quantities, and m_{CFD} reduced to a fast boundary-layer code. As such, no real computational bottleneck existed during the calibration phase.

The calibration outcome is a discrete approximation of the joint posterior probability distribution of the parameters, which is then available for the prediction of new (unobserved) scenarios. Let Δ be a quantity of interest to be predicted for a new scenario \tilde{S} , for which we do not have data. The QOI may be a scalar, vector, or functional quantity derived from the flow state. Because m_{CFD} is a model for Δ , we write

$$\Delta \simeq H_{\Delta} \circ m_{\text{CFD}}(\tilde{S}; M, \theta) \quad (3)$$

where, analogous to H_z , H_{Δ} is an observation operator extracting Δ from the full flow state, M is the closure model adopted for the prediction, and \tilde{S} is the prediction scenario. Equation (3) is a prediction based on a single choice for M and the associated parameters, i.e., a deterministic prediction. A stochastic prediction accounting for parameter uncertainty is obtained by propagating the posterior distributions for θ through Eq. (3). This, however, does not account for the fact that different distributions may be obtained by calibrating the model against different scenarios, or for the fact that multiple alternative closure models M may be used. To estimate the effect of these uncertainties, we build the full BMSA predictive distribution of Δ for a set of alternative conceptual models $\mathcal{M} = (M_1, M_2, \dots, M_i, \dots, M_I)$ under different calibration scenarios $\mathcal{S} = (S_1, S_2, \dots, S_k, \dots, S_K)$ for which we have data $\mathcal{Z} = (\mathbf{z}_1, \mathbf{z}_2, \dots, \mathbf{z}_k, \dots, \mathbf{z}_K)$ [20,22]:

$$p(\Delta|\tilde{S}, \mathcal{Z}, \mathcal{M}, S) = \sum_{k=1}^K \sum_{i=1}^I p(\Delta|\tilde{S}, \mathbf{z}_k, M_i, S_k) p(M_i|\mathbf{z}_k, S_k) p(S_k) \quad (4)$$

Equation (4) is an average of the $I \times K$ posterior predictive distributions (PPDs) $p(\Delta|\tilde{S}, \mathbf{z}_k, M_i, S_k)$. These are weighted by the posterior model probabilities $p(M_i|\mathbf{z}_k, S_k)$ and by scenario probabilities $p(S_k)$. The PPDs are obtained by marginalizing Δ over the posterior distributions of the parameters:

$$p(\Delta|\tilde{S}, \mathbf{z}_k, M_i, S_k) = \int p(\Delta|\tilde{S}, M_i, S_k, \theta) p(\theta|\mathbf{z}_k, M_i, S_k) d\theta \quad (5)$$

In simpler terms, this amounts to propagating the $I \times K$ posterior distributions $p(\theta|\mathbf{z}_k, M_i, S_k)$ through the new scenario \tilde{S} by a suitable uncertainty quantification method.

The posterior model probabilities, on the other hand, reflect how well model M_i fits the data over the support of the prior. They can be determined from a separate application of Bayes's rule, i.e.,

$$p(M_i|\mathbf{z}_k, S_k) = \frac{p(\mathbf{z}_k|M_i, S_k)p(M_i|S_k)}{\sum_{j=1}^I p(\mathbf{z}_k|M_j, S_k)p(M_j|S_k)} \quad (6)$$

where $p(M_i|S_k)$ are the prior model probabilities (generally modeled as equiprobable). Note that $p(\mathbf{z}_k|M_i, S_k)$ is the evidence for model M_i and scenario S_k , which was previously introduced in Eq. (2). Thus, in case of a model ensemble, the denominator of Eq. (2) is not ignored and is computed via

$$p(\mathbf{z}_k|M_i, S_k) = \int p(\mathbf{z}_k|M_i, S_k, \theta) p(\theta|M_i, S_k) d\theta \quad (7)$$

The first two moments of $p(\Delta|\tilde{S}, \mathcal{Z}, \mathcal{M}, S)$ can be derived directly from Eq. (4) and read as follows [20,23]:

$$\mathbb{E}[\Delta|\tilde{S}, \mathcal{Z}, \mathcal{M}, S] = \sum_{i=1}^I \sum_{k=1}^K \mathbb{E}[\Delta|\tilde{S}, \mathbf{z}_k, M_i, S_k] p(M_i|\mathbf{z}_k, S_k) p(S_k) \quad (8)$$

$$\begin{aligned} \mathbb{V}[\Delta|\tilde{S}, \mathcal{Z}, \mathcal{M}, S] &= \sum_{i=1}^I \sum_{k=1}^K \mathbb{V}[\Delta|\tilde{S}, \mathbf{z}_k, M_i, S_k] p(M_i|\mathbf{z}_k, S_k) p(S_k) \\ &+ \sum_{i=1}^I \sum_{k=1}^K \left(\mathbb{E}[\Delta|\tilde{S}, \mathbf{z}_k, M_i, S_k] - \mathbb{E}[\Delta|\tilde{S}, \mathcal{Z}, \mathcal{M}, S] \right)^2 \\ &\times p(M_i|\mathbf{z}_k, S_k) p(S_k) \\ &+ \sum_{k=1}^K \left(\mathbb{E}[\Delta|\tilde{S}, \mathcal{Z}, \mathcal{M}, S_k] - \mathbb{E}[\Delta|\tilde{S}, \mathcal{Z}, \mathcal{M}, S] \right)^2 p(S_k) \end{aligned} \quad (9)$$

where

$$\mathbb{E}[\Delta|\tilde{S}, z_k, \mathcal{M}, S_k] := \sum_{i=1}^I \mathbb{E}[\Delta|\tilde{S}, z_k, M_i, S_k] p(M_i|z_k, S_k)$$

is the BMA prediction within scenario S_k . Equation (9) shows that the posterior predictive distribution variance for Δ consists of three terms: the first term is called the within model, within scenario variance; and it accounts for predictive uncertainties due to the residual parameter variability after calibration of a model M_i under a scenario S_k . The second one is called the between model, within scenario variance. It is large if the models, using the posterior parameter distributions originating from the same calibration scenario, provide different predictions for the new configuration. It can therefore be considered as a measure for model error. The last term is the between scenario variance, which accounts for the fact that different calibration scenarios lead to different estimates of the parameters. Thus, when applying the BMSA model to a prediction scenario \tilde{S} for which it is not calibrated, this uncertainty should be taken into account.

B. Implementation of BMSA for CFD Problems

In this paper, we focus on the prediction step, and we refer the reader to [5,23] for details about the calibration step. All flow predictions presented in the following are based on the posterior parameter distributions previously computed for a class of flat-plate boundary-layer flows subject to various external pressure gradients [23]. These constitute a database of posterior probability distributions, which are available for propagation through new flow configurations. The interested reader may download the samples of the posterior θ distributions used in the following applications from [30]. Because these parameter estimates were determined for wall-bounded flow configurations, we expect these may be used to predict other (more complex) wall-bounded flows. The validity of this working assumption will be assessed in subsequent sections.

The calibration step also provides information about the posterior model probabilities [Eq. (6)]. Indeed, for each model and calibration scenario, it is possible to compute the evidence by Monte Carlo integration of Eq. (7). For instance, for the cheap flat-plate boundary-layer scenarios, the evidence is computed by drawing a large number of samples ($\theta_n, n = 1, \dots, N$) from the prior $p(\theta|M_i, S_k)$ and by approximating Eq. (7) as

$$p(z_k|M_i, S_k) \approx \frac{1}{N} \sum_{n=1}^N p(z_k|M_i, S_k, \theta_n) \quad (10)$$

The posterior model weights can now be calculated through the simple algebraic relation [Eq. (6)]; the results of which we tabulated in the Appendix. It should be noted that computing the evidence using samples from the prior is not always feasible. Convergence of the Monte Carlo (MC) estimate [Eq. (10)] will become slow if the region where the likelihood has high probability is significantly different from the region of high prior probability content [31]. In this case, more advanced sampling techniques will be required; see, e.g., [29,32].

The prediction step involves 1) propagating posterior parameter distributions for each competing model through the prediction scenario \tilde{S} ; 2) assigning a suitable probability mass function to the scenarios S_k ; and 3) applying the BMSA relations [Eq. (4)] and/or Eqs. (8) and (9) to obtain the predictive posterior distribution and/or its moments for the QOI Δ .

Steps 2 and 3 only involve a negligible or small computational load. The computational bottleneck is represented by step 1, which requires running the CFD model on scenario \tilde{S} for all models in \mathcal{M} and for a large number of samples in each posterior distribution $p(\theta|z_k, M_i, S_k)$, leading to $I \times K$ stochastic estimates of Δ . Because each CFD simulation is likely to be expensive itself, propagation by means of Monte Carlo sampling is unacceptably costly. The computational cost can be greatly alleviated by using surrogate

models (see, e.g., [33]), yet a significant number of CFD runs [$\mathcal{O}(100)$ or higher] is still required, even when using advanced surrogate modeling techniques. For this reason, in Sec. III.D, we introduce an approximation that drastically reduces the computational cost associated to the prediction step. In the next section, we complete the description of the BMSA by discussing the choice of the scenario probability mass function (step 2).

C. Weighting the Scenarios

Whereas the posterior model probabilities $p(M_i|S_k, z_k)$ were informed from the calibration data z_k , the scenario probabilities $p(S_k)$ were of a predictive nature and incorporated uncertainty for the fact that the MAP estimates were applied to a predictive scenario \tilde{S} for which they were not calibrated. Ideally, experimental data from \tilde{S} would be available, which we could use to inform $p(S_k)$. However, because, in many engineering applications of CFD, this would not be the case, we assumed we only had data coming from the K calibration scenarios S_k . Instead of informing on data, we specified $p(S_k)$, based on model agreement per S_k . Specifically, following [23], we set the following:

$$p(S_k) := \frac{\xi_k^{-p}}{\sum_{j=1}^K \xi_j^{-p}}, \quad \xi_k = \sum_{i=1}^I \left\| \mathbb{E}[\Delta|\tilde{S}, z_k, M_i, S_k] - \mathbb{E}[\Delta|\tilde{S}, z_k, \mathcal{M}, S_k] \right\|_2 \quad \forall S_k \in \mathcal{S} \quad (11)$$

Here, ξ_k measures model agreement by means of an L_2 -normed variation around the BMA expectation $\mathbb{E}[\Delta|\tilde{S}, z_k, \mathcal{M}, S_k]$. If all turbulence models show a high level of agreement regarding the value of Δ when using the posteriors calibrated on S_k , such a scenario is given a high probability, and vice versa. The rationale is that, if a given S_k is similar to the predictive \tilde{S} at hand, the models are expected to give similar predictions, given that the parameter distributions are calibrated on the same data z_k . Additionally, $p \in \mathbb{N}_0$ is an integer that controls the degree to which variation is penalized. For $p = 0$, we obtain a uniform distribution and, for higher values of p , we effectively damp the results coming from those scenarios with a low level of model agreement ξ_k . In Sec. IV, we carry out numerical experiments to demonstrate that ξ_k indeed represents a good model for the true discrepancy between the BMSA prediction and the data, and we discuss the role of the exponent p . Finally, note that Eq. (11) requires a minimum of two models; the use of one model will always yield a uniform distribution. With just a single model, one might still use the variability over S_k to inform the $p(S_k)$, or simply rely on expert opinion.

A valid criticism of Eq. (11) is that the "best" S_k will not be favored if all models in \mathcal{M} for a given "wrong" S_k produce predictions that are incorrect in a very similar manner. Due to the fact that we do not allow ourselves any reference data for the predictive flow scenario, we cannot fully exclude the possibility of such a situation. However, we can suggest means to decrease its risk through 1) selecting a larger set of diverse models of different fidelity, which are unlikely to agree with each other; 2) selecting a relevant set of calibration scenarios because, in previous research [23], it was found that Eq. (11) did favor S_k similar to \tilde{S} if the flow topology was comparable; and 3) limiting the value of p , which gave the user control over how much $p(S_k)$ was allowed to deviate from a uniform distribution.

D. Speeding up BMSA Predictions: MAP Approximation of the Posterior Parameter Distributions

A way to drive the estimate of the individual predictive distributions $p(\Delta|\tilde{S}, z_k, M_i, S_k)$ to an acceptable computational cost consists of approximating the marginal posterior probability distributions $p(\theta|z_k, M_i, S_k)$ with Dirac- δ functions at their maximum a posteriori (MAP) values:

$$\theta_{i,k}^{\text{MAP}} := \underset{\theta}{\text{argmax}} p(\theta|z_k, S_k, M_i) \quad (12)$$

so that

$$p(\boldsymbol{\theta}|z_k, S_k, M_i) \simeq \delta(\boldsymbol{\theta} - \boldsymbol{\theta}_{i,k}^{\text{MAP}}) \quad (13)$$

The consequence of this approximation is to neglect the effect of the within model, within scenario variance. The PPD variance still includes the effect of multiple models and scenarios. Note that, if perfectly plentiful data are available in the training scenarios (and the models are able to fit the data exactly for some values of the closure coefficients), then the $p(\boldsymbol{\theta}|S_k, M_i, z_k)$ will tend toward Dirac δ functions. So, one way to think of this approximation is as neglecting the effect of imperfect training. The MAP estimates (see the Appendix) are estimated from kernel-density estimates constructed with Markov Chain Monte Carlo (MCMC) samples of previous research [30]; see also Fig. 1. Although this might only be an approximation to each individual MAP value, it is the spread of different MAP values that is important in our approach; see the discussion in Sec. IV.A.

Substituting Eq. (13) into Eq. (5) leads to an approximation of the posterior predictive distribution $p(\Delta|\tilde{S}, \mathcal{Z}, \mathcal{M}, S) \simeq \hat{p}(\Delta|\tilde{S}, \mathcal{Z}, \mathcal{M}, S)$ by

$$\begin{aligned} \hat{p}(\Delta|\tilde{S}, \mathcal{Z}, \mathcal{M}, S) \\ = \sum_{i=1}^I \sum_{k=1}^K \delta(\Delta - \Delta_{\text{CFD}}(\tilde{S}; M_i, \boldsymbol{\theta}_{i,k}^{\text{MAP}})) p(M_i|S_k, z_k) p(S_k) \end{aligned} \quad (14)$$

where we define $\Delta_{\text{CFD}}(\tilde{S}) := H_{\Delta} \circ m_{\text{CFD}}(\tilde{S})$, and we use the fact that propagating a δ distribution requires running m_{CFD} only at $\boldsymbol{\theta} = \boldsymbol{\theta}_{i,k}^{\text{MAP}}$, returning a δ distribution centered at $\Delta_{\text{CFD}}(\tilde{S})$ for the output. The approximate PPD is then reduced to a weighted sum of $I \times K$ δ -functions [one at each prediction of $\Delta_{\text{CFD}}(\tilde{S})$ for each model] and each scenario's MAP estimate of $\boldsymbol{\theta}$. The cost of evaluating the PPD is then $I \times K$ runs of $\Delta_{\text{CFD}}(\tilde{S})$. Finally, the mean and variance of Eq. (14) are easy to evaluate using the properties of δ functions, and it contains terms from our database [$p(M_i|S_k, z_k)$ and $\boldsymbol{\theta}_{i,k}^{\text{MAP}}$], a user choice $p(S_k)$, and the RANS output for Δ via m_{CFD} :

$$\mathbb{E}[\Delta|\tilde{S}, \mathcal{Z}, \mathcal{M}, S] = \sum_{i=1}^I \sum_{k=1}^K \Delta_{\text{CFD}}(\tilde{S}; M_i, \boldsymbol{\theta}_{i,k}^{\text{MAP}}) p(M_i|S_k, z_k) p(S_k) \quad (15)$$

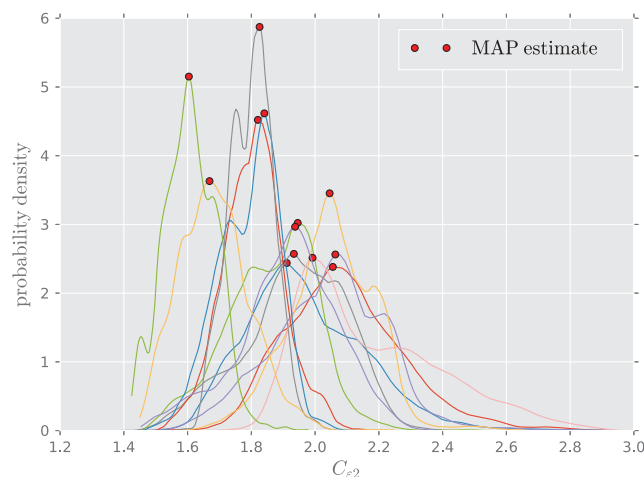


Fig. 1 All marginal posterior distributions of $C_{\epsilon 2}$ (obtained from kernel-density estimates using the MCMC samples of [23]) and the corresponding MAP estimates.

$$\begin{aligned} \mathbb{V}[\Delta|\tilde{S}, \mathcal{Z}, \mathcal{M}, S] &= \sum_{k=1}^K \sum_{i=1}^I \left[\Delta_{\text{CFD}}(\tilde{S}; M_i, \boldsymbol{\theta}_{i,k}^{\text{MAP}}) - \mathbb{E}[\Delta|\tilde{S}, z_k] \right]^2 \\ &\times p(M_i|S_k, z_k) p(S_k) + \sum_{k=1}^K \left(\mathbb{E}[\Delta|\tilde{S}, z_k] - \mathbb{E}[\Delta|\tilde{S}, z] \right)^2 p(S_k) \end{aligned} \quad (16)$$

Note that, compared to Eq. (9), the PPD variance for Δ now contains only two terms: the between model, within scenario variance; and the between scenario variance. The effect of the MAP approximation on the PPD variance is investigated in Sec. IV.

IV. Preliminary Validation

In this section we use our numerical boundary-layer flow database [23] along with experimental data from [34] for the preliminary validation of two key ingredients of the present BMSA formulation, namely, the MAP approximation and the scenario weighting. The boundary-layer flows considered in the present calculations and the corresponding nomenclature are described in the Appendix.

A. Influence of the MAP Approximation

The MAP approximation ignores the effect of imperfect training within each calibration scenario (i.e., it ignores the variance of each individual posterior). As an example, consider the results of Fig. 1, where all 14 posterior distributions of the coefficient $C_{\epsilon 2}$ (of the $k - \epsilon$ model; see Appendix) and the corresponding MAP estimates are plotted. The variance of these marginals is not considered small due to the fact that, even at the best model parameters, there is still model inadequacy that will prevent the posteriors from approaching delta distributions [24,26,29]. Moreover, not all parameters will be equally sensitive to the reference data. It was previously observed [5,23] that parameters with low Sobol indices would yield posteriors that did not deviate much from our (uniform) prior. As such, the MAP approximation might seem to neglect a large amount of uncertainty. However, because we consider 14 different calibration scenarios, and because the modes of the posteriors significantly disagree on the most likely value of $\boldsymbol{\theta}$, the MAP approximations still span a large section of the $\boldsymbol{\theta}$ domain; see, again, Fig. 1 for an example. Hence, the MAP approximation is of the least influence when this span is sufficient to yield an envelope on the QOI that is similar in size to the full posterior PPD variance, which is obtained by propagating all posterior $\boldsymbol{\theta}$ distributions. It should be noted, however, that this will only hold for lower-order statistical moments; all information contained in the tails of the posteriors will be lost in the MAP approximation.

We can evaluate the effect of the MAP approximation on the boundary-layer flows of the calibration phase by computing the posterior standard deviation of the full BMSA method and the current proposed approach of Sec. III.D. Figure 2 shows the predictive results for an unseen boundary layer with uniform $p(S_k)$, where Δ is a u^+ profile, defined as $u^+ := \langle U \rangle / u_{\tau}$. Here, $\langle U \rangle$ is the mean streamwise velocity and u_{τ} is the friction velocity. Precisely, we use posteriors from the remaining 13 boundary-layer scenarios in Table A6 (Appendix) to predict case 1400 [34]. Note that the total variability in Δ is fairly similar in both cases. Due to the lack of a within model, within scenario component in the MAP approach, a larger part of the standard deviation in Δ is lumped into the between scenario component. We repeat this procedure for a number of unseen boundary layers, and we obtain similar results. Thus, for those cases considered where we can compute the full BMSA PPD standard deviation, we do not observe a significant underestimation of the posterior predictive standard deviation when the MAP approach is used.

B. Influence of the Scenario Weighting

Equation (11) raises the following question: Is ξ_k a good measure for the true model error contained in each S_k ? Let us first define the true model error as follows:

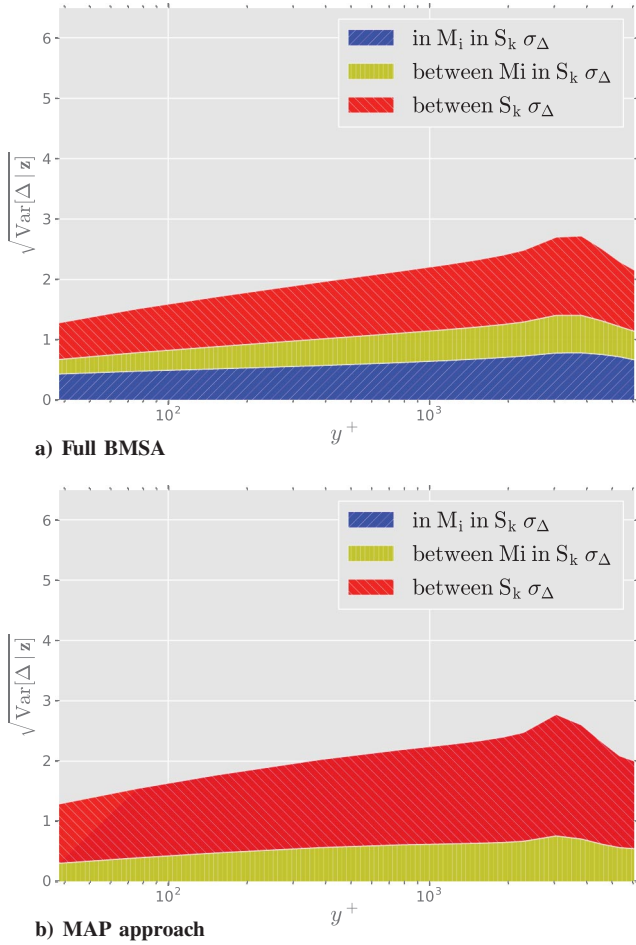


Fig. 2 The posterior standard-deviation of $\Delta = u^+$ versus y^+ for the full BMSA method (9) and the simplified MAP approach (16).

$$\tilde{\xi}_k := \sum_{i=1}^I \left\| H_z \circ m_{\text{CFD}}(\tilde{S}; M_i, \theta_{i,k}^{\text{MAP}}) - z_k \right\|_2$$

where, in our case, the z_k are experimental u^+ profiles. We can then evaluate its proximity to our error model ξ_k by performing a leave-one-out validation analysis on the K calibration scenarios. Note that a given MAP estimate $\theta_{i,k}^{\text{MAP}}$ is not calibrated on the data of the other $K - 1$ calibration scenarios S_j , $j \in \{1, \dots, K\} \setminus \{k\}$. The scenarios are roughly ordered from “easy” zero-pressure gradient scenarios at $k = 1$ to the most difficult, highly adverse scenarios near $k = K$; see the Appendix for a more complete description. By using each $\theta_{i,k}^{\text{MAP}}$ to compute u^+ in these remaining $K - 1$ scenarios, we can evaluate both ξ_k and $\tilde{\xi}_k$ due to the availability of data. The results are shown in Fig. 3, where the dotted line corresponds to perfect agreement $\xi_k = \tilde{\xi}_k$. Each subplot shows the results of a single MAP estimate applied to all other scenarios. In each of the k subplots ($k = 1, \dots, 14$), the MAP estimates are fixed to those obtained from calibration scenario S_k . The MAP estimates are then used to compute both the true error $\tilde{\xi}_k$ and the modeled error ξ_k [Eq. (11)] when applied to prediction scenarios S_j , $j \in \{1, \dots, K\} \setminus \{k\}$. The true errors $\tilde{\xi}_k$ are computed using the experimental u^+ data from [34]. Note that, in general, the results lie close to the $\xi_k = \tilde{\xi}_k$ line. However, MAP estimates calibrated under easy zero or favorable pressure gradient scenarios can yield discrepancies between ξ_k and $\tilde{\xi}_k$. More specifically, we observe such discrepancies when using a MAP estimate calibrated under an easy scenario to predict a QOI under a difficult scenario; see, e.g., the results of applying $\theta_{i,1}^{\text{MAP}}$ to predict the u^+ profile of S_{14} . On the other hand, MAP estimates that are

calibrated under the most difficult strongly adverse scenarios perform well across all S_k ; see the results for $\theta_{i,13}^{\text{MAP}}$ and $\theta_{i,14}^{\text{MAP}}$.

The parameter p of Eq. (11) is user specified. To estimate its value, we use a similar leave-one-out analysis and the experimental data from the calibration scenarios. In this case, we fix a scenario S_k and use the remaining $\theta_{i,j}^{\text{MAP}}$, $j \in \{1, \dots, K\} \setminus \{k\}$ to predict the QOI for a given value of p . Let us define a relative error in the BMSA prediction as

$$\epsilon_k^{\text{rel}} := \frac{\|\mathbb{E}[\Delta|z] - z_k\|_2}{\|z_k\|} \times 100\% \quad (17)$$

For all S_k , we can now examine the behavior of Eq. (17) as a function of p . The results are depicted in Fig. 4. For most S_k , the relative error is either minimized or reaches a plateau for $p \in \{1, 2, 3\}$. Based on these results, we will set $p = 2$ in predictive cases where no experimental data are available.

V. Assessment of BMSA for Selected Flow Cases

In this section, the MAP-based BMSA predictive methodology is assessed against selected flow cases, namely, separated incompressible flow and three-dimensional (3-D) transonic flow past a wing. The considered applications are rather different from our calibration scenarios, although they still involve boundary layers subject to variable pressure gradients, and they exhibit features beyond the limits of applicability of linear RANS models, due to the strong nonequilibrium effects. As such, they represent severe tests for the proposed approach.

A. Flow over Periodic Hills at $Re_H = 5600$

The flow over a series of periodically arranged hills deals both with flow separation on the curved surface of the hills and reattachment between the hills. The test case is known to be especially challenging for linear eddy viscosity models, which are not able to predict the mean effect of the unsteady fluctuation of the separation and reattachment points correctly.

The periodicity of the hill geometry is mimicked with periodic boundary conditions at the inlet and outlet and no-slip conditions at the walls. A volume forcing is applied to each cell, which maintains a bulk velocity of $U_b = 1.0$ between the hill’s crest and the upper surface. The considered Reynolds number of $Re_H = 5600$ based on the hill height H and bulk velocity between the hill’s crest and the upper surface is maintained by a volume forcing. The CFD simulations are performed using OpenFOAM’s `simpleFoam` solver [35]. We use validation data of the mean flowfield from Breuer et al. for comparison [36]. Three turbulence models are used: Spalart–Allmaras; Launder–Sharma $k - \epsilon$; and Wilcox (2006) [1] $k - \omega$, with $y^+ \leq 1.0$. A mesh convergence study is conducted for each model using baseline coefficients, resulting in meshes with sizes of 100×110 (Spalart–Allmaras and Launder–Sharma $k - \epsilon$) and of 150×140 (Wilcox [1] $k - \omega$) cells in the $x \times y$ direction, respectively.

The baseline simulations for the three models show the expected behavior as reported in the literature (for a larger Reynolds number Re): whereas both the Spalart–Allmaras and the Wilcox [1] $k - \omega$ overpredict the size of the recirculation zone, characterized by a zero-velocity component close to the wall, the Launder–Sharma $k - \epsilon$ underpredicts this flow feature. For S_{14} , the simulation using the Wilcox [1] $k - \omega$ did not converge, so this scenario is excluded from the set, leading to only 13 scenarios being used for the BMSA predictions.

The BMSA expectation $\mathbb{E}[\Delta|\tilde{S}, z]$ of the streamwise velocity, as shown in Fig. 5, overpredicts the recirculation zone and gives similar velocity profiles for $x = 3.0$ and 4.0 close to the lower surface. Especially for $x = 0.0$, the expectation does not capture the local maximum of the velocity close to $y/H = 1.0$, i.e., at the hill’s crest. Throughout the different locations, the expectation shows differences as compared to the DNS for the upper part of the velocity profile, which might be due to a compensation effect caused by the fixed mass flow.

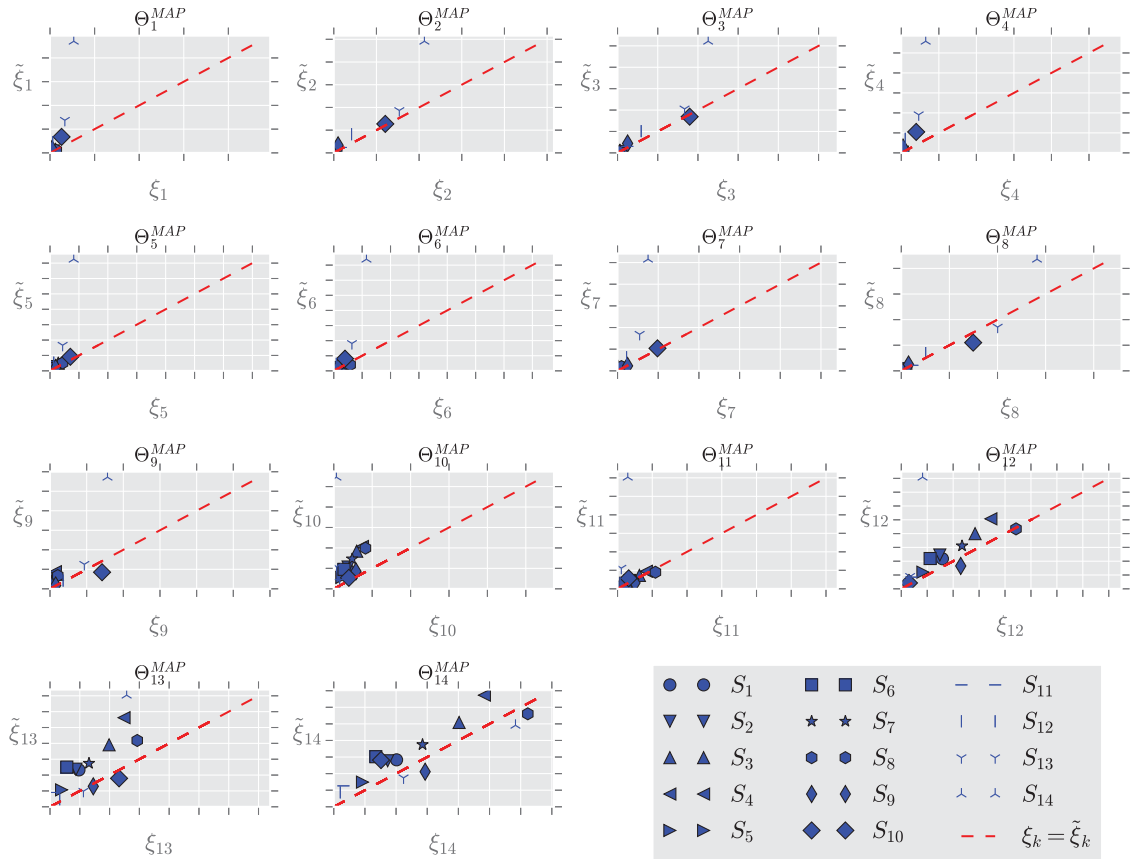


Fig. 3 The results of the cross validation study.

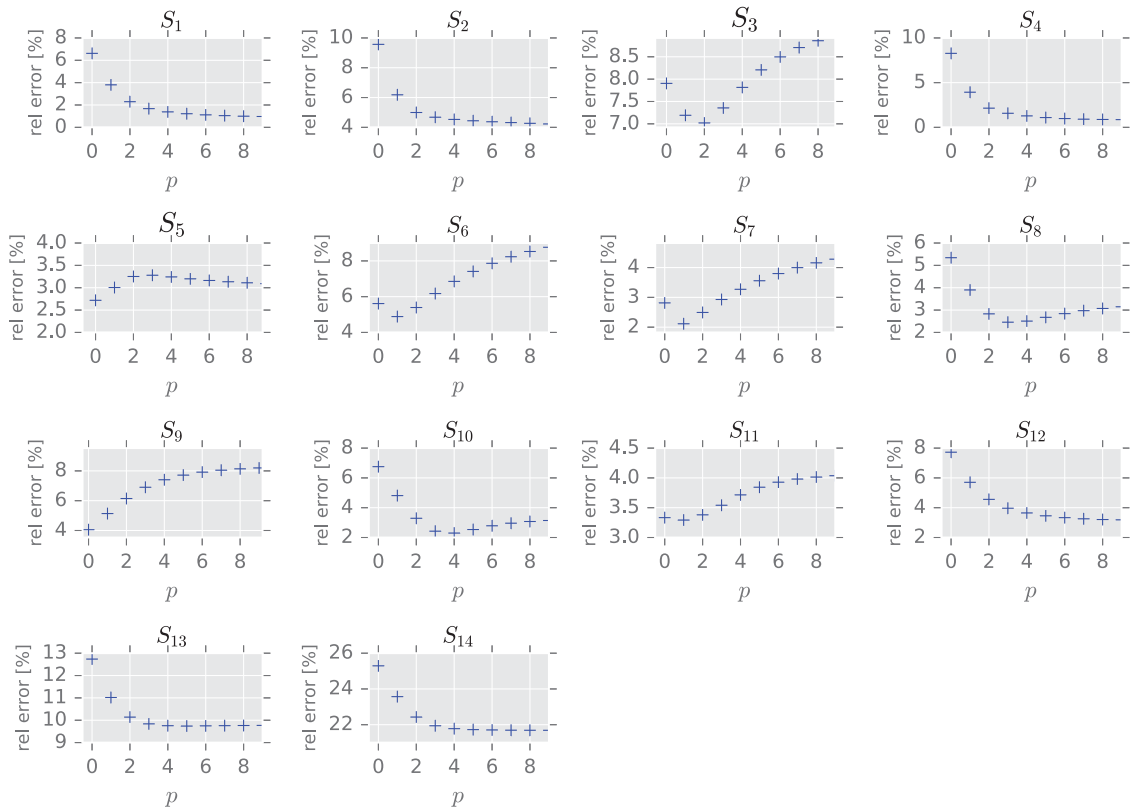


Fig. 4 Relative (rel) error in the BMSA prediction of u^+ for all K scenarios S_k .

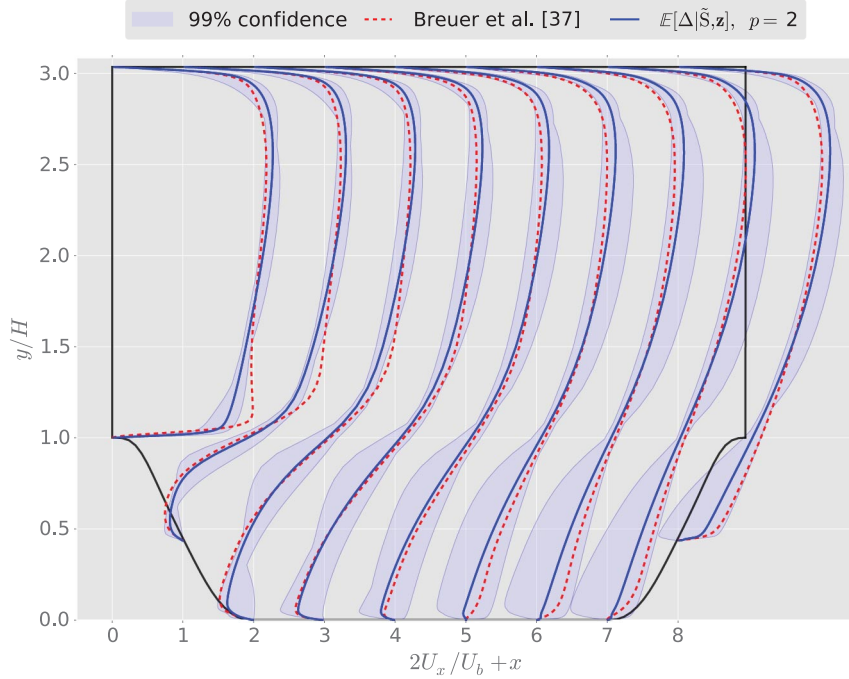


Fig. 5 BMSA for the periodic hill flow.

The 99% confidence interval captures the DNS data for $x \geq 3$ but not the region close to the upper wall for $x \geq 5$ and the local velocity maxima in the area of the free-shear layer in the leeward region of $x = 0$ to 2.0 . Interestingly, for $x \leq 3.0$, when the range of the confidence interval shrinks locally in the y/H direction, the DNS is still inside. However, this pattern is not the same for every y/H position; e.g., at $x = 2.0$, the expectation and the DNS match for $0.5 \leq y/H \leq 1$, but the confidence interval is large. Interestingly, in the reattachment region between the two hills, where the case is similar to a flat plate, the confidence interval is able to capture the DNS data consistently.

In general, the application of BMSA to this test case demonstrates the aforementioned fact that the used linear eddy viscosity models suffer from restrictions, which inhibit the reproduction of effects due to, e.g., streamline curvature as well as Reynolds stress anisotropy. These are essential characteristics of this challenging test case. Adding second-order closures to \mathcal{M} might remedy this deficiency at increased computational cost. However, the BMSA confidence interval captures most of the modeling error, showing robustness of the method, even for this challenging test case.

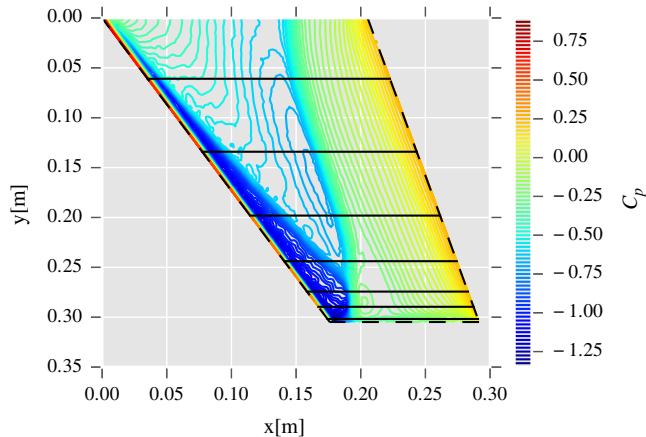
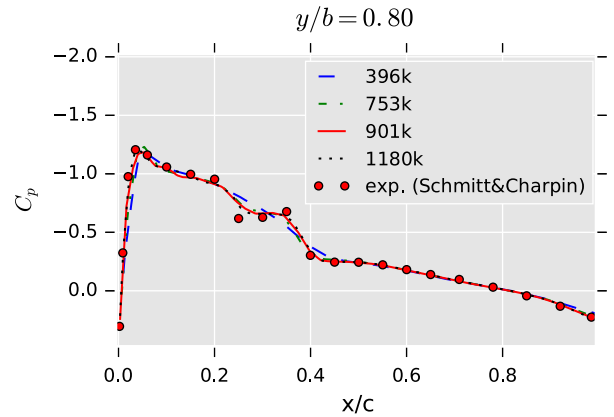


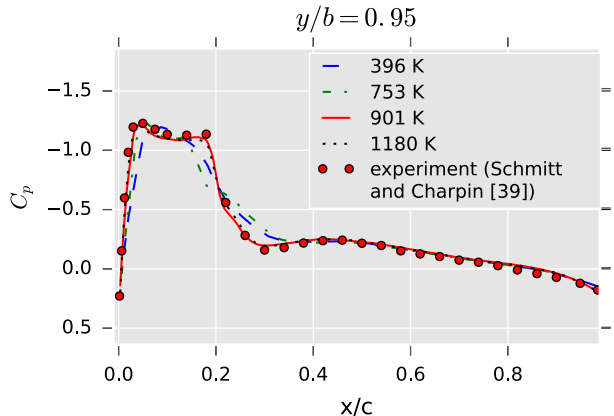
Fig. 6 Typical C_p distribution on the suction side of the ONERA M6 wing. The black lines correspond to the $y/b = [0.2, 0.44, 0.65, 0.80, 0.90, 0.95, 0.99]$ stations, where C_p data are available from [38].

B. Transonic Flow over the ONERA M6 Swept Wing

The second application of our boundary-layer trained BMSA is the transonic flow over the ONERA M6 wing. This is a swept wing based on the ONERA D airfoil with no twist. The M6 wing is known to



a) The C_p distributions at $z/b = 0.8$



b) The C_p distributions at $z/b = 0.95$

Fig. 7 C_p distributions of the four meshes at two spanwise locations. All computations done using the MAP estimates of calibration case 1400.

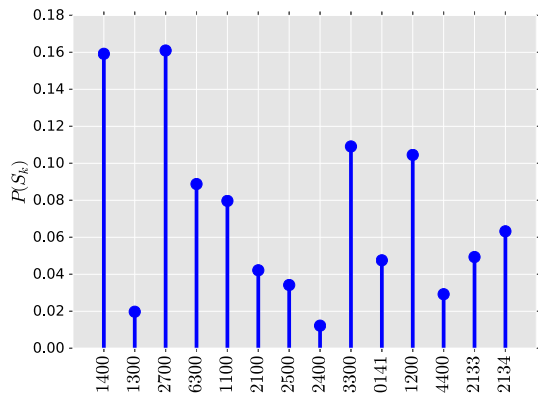
produce complex physics at transonic Mach numbers. See, for instance, the pressure distribution depicted in Fig. 6. Due to the configuration of local supersonic regions [37], a λ shock is formed where the double shock merges into a single one between $y/b = 0.8$ and $y/b = 0.9$.

A well-known CFD validation case (see, e.g., [37,39,40]) involves the ONERA M6 wing at Mach 0.835 and a Reynolds number (based on the freestream conditions and the mean aerodynamic chord) of 11.72×10^6 , with an angle of attack of 3.06 deg and a 0.0 deg sideslip. The pressure and temperature at the far field are given by $p_\infty = 315980$ Pa and $T_\infty = 255.5$ K. The CFD calculations are performed using Ansys Fluent, using the pressure-based solver. More details on the numerical setup can be found in [41,42]. For these conditions, experimental pressure data are available from Schmitt

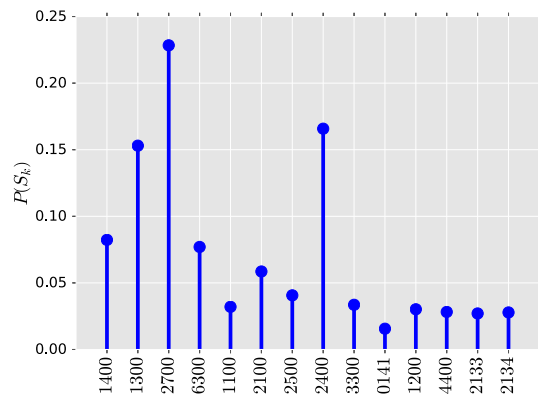
and Charpin [38] at several y/b stations. The error in the reported pressure data is $\Delta C_p = \pm 0.02$.

Before beginning the BMSA procedure, we performed a qualitative comparison of the C_p distributions using the MAP estimates of the 1400 case on four unstructured meshes of increasing size, namely, $\{396, 753, 901, 1180\} \times 10^3$ elements. The results at $z/b = 0.80$ and $z/b = 0.95$ are shown in Fig. 7. Note that the coarsest mesh smears the double shock at $y/b = 0.80$, and both meshes 1 and 2 smear the shock at $y/b = 0.95$. Between the two finest meshes, we observed little variation; we therefore selected mesh 3 to perform the sampling with MAP estimates.

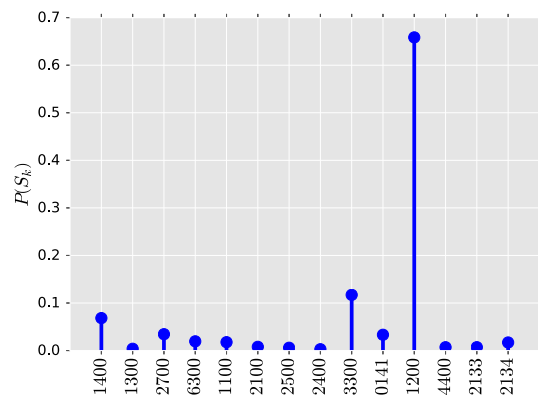
Our model set for this case consists of the $k - \varepsilon$ and SA models. We computed the mean C_p prediction [Eq. (15)] and the standard deviation based on Eq. (16) for the entire suction side of the M6 wing.



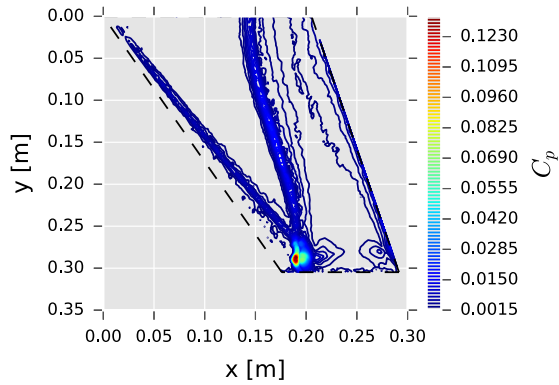
a) The $p(S_k)$ distribution for the entire wing



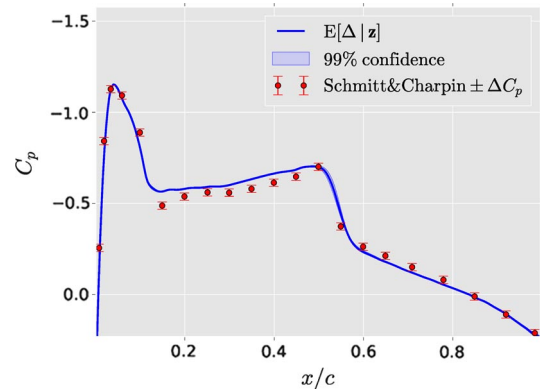
c) The $\mathbb{P}(S_k)$ distribution at $y/b = 0.44$



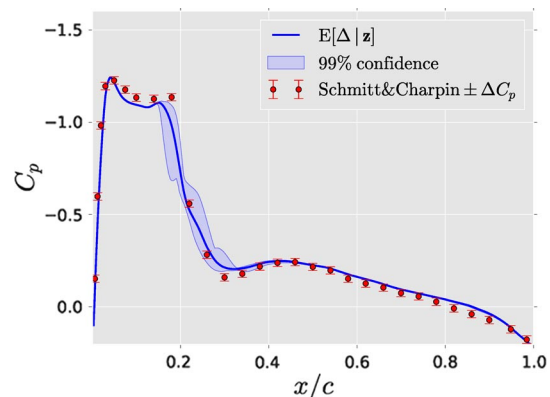
e) The $\mathbb{P}(S_k)$ distribution at $y/b = 0.95$



b) The standard deviation of Eq. (16)



d) The BMSA prediction at $y/b = 0.44$ plus 99% confidence region



f) The BMSA prediction at $y/b = 0.95$ plus 99% confidence region

Fig. 8 Results for the ONERA M6 wing.

The mean was very similar to the results of Fig. 6. More interesting was the uncertainty in the prediction, depicted in Fig. 8b. From this standard deviation, it became clear that the uncertainty of the RANS prediction was localized in the region of the λ shock, especially where the two shocks merged.

The corresponding $p(S_k)$ distribution is shown in Fig. 8a. Note that the distribution favors the results of MAP estimates from zero (1400) and favorable (2700) calibration scenarios, as well as two adverse cases (3300 and 1200). This might be explained by the fact that the transonic flow experiences a wide range of pressure gradients, at different locations of the wing. Perhaps the weights $p(S_k)$ should ideally reflect the inhomogeneous nature of the uncertainty rather than computing a scalar $p(S_k)$ for each k and assuming it is applicable throughout the entire flowfield. To investigate, we compute the BMSA prediction along different y/b stations of the wing. For each station, taking the local C_p distribution as the QOI, we recompute $p(S_k)$. This allows us to build up a picture of how $p(S_k)$ varies from the wing root to the tip. A selection of results, at y/b stations where we have experimental validation data, are displayed in Figs. 8c–8f. First, notice that the amount of uncertainty at $y/b = 0.44$ is very low, which is a result that could already be inferred from Fig. 8b. The $p(S_k)$ distribution at this station displays a preference for mostly those results computed using zero or favorable pressure-gradient MAP estimates. Note, however, that the final C_p distribution is insensitive to $\mathbb{P}(S_k)$ in cases of very low uncertainty, seeing that all S_k yield very similar predictions. Other computed $p(S_k)$ distributions are comparable, up until the neighborhood of $y/b = 0.95$, where the results are quite different. Here, a relatively large amount of uncertainty is present, accompanied by a different $p(S_k)$ distribution. There is a preference for the pressure computed with MAP estimates coming from a strongly adverse calibration scenario (namely, scenario 1200). These results suggest that incorporating a spatial dependence in $\mathbb{P}(S_k)$ does indeed reflect the local flow physics better. Specifying $p(S_k)$ locally through Eq. (11) assumes that there is no spatial correlation.

VI. Conclusions

A Bayesian model-scenario averaging methodology was applied to estimate turbulence modeling uncertainties in RANS computations. Specifically, the goal of this paper was to assess the predictive capability of a BMSA model, trained on experimental velocity profiles for a set of flat-plate boundary layers, when predicting other, more computationally expensive flow problems. Two severe validation cases were considered: namely, the separated flow over periodic hills and a shocked transonic flow over a 3-D wing. These contained physics that were not present during the training phase, such as compressibility effects and separation. The full BMSA approach required the propagation of a set of posterior distributions, which proved to be computationally intractable for industrial-relevant test cases. It was therefore proposed to approximate the posterior distributions with Dirac- δ functions centered at the maximum a posteriori estimates of the posterior distributions. This was the most drastic cost reduction possible, with just one code evaluation per closure model: calibration scenario pair.

The main advantage of an approach such as BMSA is that one can make predictions with quantified uncertainty. Such information is not available with the baseline models, and it provides insight into where, and to what extent, the closure models fail to be trustworthy. The confidence region generated by BMSA thus provides meaningful bounds on the QOI. In the selected cases, an overlap was observed between the confidence intervals and the reference data, especially when the local flow physics resembled the attached boundary layers of the calibration phase. Where there was no overlap, the discrepancy between the propagated model-scenario pairs was small, which might be remedied by including additional closure models in the set, e.g., nonlinear eddy viscosity models.

Appendix: Tables of Map Estimates, Posterior Model Probabilities, and Calibration Cases

Here, we report the MAP estimates of the closure coefficients for the three turbulence models of Sec. II [Tables A1–A3, as well as the corresponding posterior model probabilities (Tables A4 and A5)]. We also give a description of the calibration cases.

In the case of the $k - \varepsilon$ mode, we use Eqs. (A1) and (A2) to fix the value of σ_ε and $C_{\varepsilon 1}$, where we set $\mathcal{P}/\varepsilon = 2.09$ for the latter; see [5] for a discussion. We use other well-known algebraic relations for the $k - \omega$ and SA models in Eqs. (A3) and (A4), respectively [1]:

$$\sigma_\varepsilon = \frac{\kappa^2}{C_\mu^{1/2}(C_{\varepsilon 2} - C_{\varepsilon 1})} \quad (\text{A1})$$

$$\left(\frac{\mathcal{P}}{\varepsilon}\right) = \frac{C_{\varepsilon 2} - 1}{C_{\varepsilon 1} - 1} \quad (\text{A2})$$

$$\alpha = \frac{\beta}{\beta^*} - \frac{\kappa^2}{2\sqrt{\beta^*}} \quad (\text{A3})$$

$$C_{w1} = \frac{C_{b1}}{\kappa^2} + \frac{1 + C_{b2}}{\sigma} \quad (\text{A4})$$

Table A1 MAP estimates of the $k - \varepsilon$ model for the different calibration scenarios

Scenario ^a	$C_{\varepsilon 2}$	C_μ	σ_k	κ
Nominal	1.92	0.09	1.0	0.41
S_1	2.0429	0.0646	1.4032	0.428
S_2	2.0556	0.0726	1.1737	0.4551
S_3	1.911	0.0655	0.7082	0.451
S_4	2.0634	0.0715	1.4205	0.4621
S_5	1.9334	0.0618	1.0796	0.3604
S_6	2.0456	0.0654	1.4156	0.3865
S_7	1.9454	0.0604	1.0314	0.4365
S_8	1.9919	0.0841	1.2869	0.4596
S_9	1.8205	0.0699	0.9999	0.36
S_{10}	1.8407	0.06	1.4067	0.3559
S_{11}	1.9373	0.0599	1.1435	0.3282
S_{12}	1.8258	0.0625	1.2562	0.3259
S_{13}	1.6687	0.0642	0.8093	0.2964
S_{14}	1.604	0.0578	0.7327	0.2902

^aThe nominal values are depicted on the first row.

Table A2 MAP estimates of the Wilcox [1] $k - \omega$ model for the different calibration scenarios

Scenario ^a	α	β_0	β^*	σ	σ^a
Nominal	0.52	0.0708	0.09	0.5	0.6
S_1	0.4557	0.0668	0.0768	0.4953	0.4107
S_2	0.4369	0.0728	0.0848	0.5186	0.5177
S_3	0.4383	0.0687	0.0828	0.5017	0.4107
S_4	0.4703	0.0737	0.0909	0.4945	0.5231
S_5	0.5906	0.0665	0.0858	0.5089	0.4094
S_6	0.6045	0.0743	0.0895	0.5057	0.5825
S_7	0.4786	0.0644	0.0784	0.4985	0.4067
S_8	0.4306	0.0738	0.0744	0.6887	0.4074
S_9	0.4946	0.0629	0.0744	0.6927	0.406
S_{10}	0.4682	0.0647	0.0844	0.5234	0.4087
S_{11}	0.592	0.069	0.0979	0.4961	0.4167
S_{12}	0.6129	0.0696	0.0904	0.5073	0.4268
S_{13}	0.592	0.0649	0.0887	0.5106	0.4147
S_{14}	0.6087	0.0644	0.1043	0.4985	0.5853

^aThe nominal values are depicted on the first row.

Table A3 MAP estimates of the SA model for the different calibration scenarios

Scenario ^a	C_{b1}	C_{b2}	C_{u1}	σ	C_{u2}	C_{u3}
Nominal	0.1355	0.622	7.1	0.67	0.3	2.0
S_1	0.1354	0.5377	7.1833	0.8009	0.3664	2.0619
S_2	0.1185	0.6152	6.881	0.602	0.349	1.8144
S_3	0.1264	0.6302	7.1017	0.5711	0.2702	2.4675
S_4	0.144	0.5629	7.1384	0.7964	0.3731	2.4636
S_5	0.1299	0.7561	7.6842	0.746	0.3682	1.7774
S_6	0.1305	0.5678	6.6114	0.658	0.2931	1.8615
S_7	0.1606	0.6559	9.0895	0.8144	0.3153	2.3111
S_8	0.1048	0.519	7.7523	0.6889	0.2468	2.047
S_9	0.1353	0.5042	8.5117	0.5256	0.3033	2.054
S_{10}	0.1693	0.6837	9.0427	0.7917	0.2384	2.0496
S_{11}	0.1286	0.5441	6.8871	0.7676	0.3671	1.5532
S_{12}	0.1214	0.7211	7.022	0.5924	0.257	1.641
S_{13}	0.1062	0.6327	7.9545	0.6648	0.2601	1.5889
S_{14}	0.0983	0.5603	6.5696	0.5643	0.2938	2.1707

^aThe nominal values are depicted on the first row.

Table A4 Posterior model probabilities $p(M_i|z_k)$ when \mathcal{M} consists of the $k - \epsilon$ and SA models^a

Scenario	$k - \epsilon$	SA
S_1	6.54763e-02	9.34524e-01
S_2	1.31256e-01	8.68744e-01
S_3	9.98800e-01	1.19985e-03
S_4	2.09486e-01	7.90514e-01
S_5	9.95836e-01	4.16372e-03
S_6	2.36294e-01	7.63706e-01
S_7	1.00000e+00	4.51629e-07
S_8	1.00000e+00	4.34707e-11
S_9	1.00000e+00	0.00000e+00
S_{10}	1.00000e+00	0.00000e+00
S_{11}	9.99867e-01	1.32751e-04
S_{12}	9.98324e-01	1.67614e-03
S_{13}	0.00000e+00	1.00000e+00
S_{14}	0.00000e+00	1.00000e+00

^aWe used a uniform prior $p(M_i)$.

Table A5 Posterior model probabilities $p(M_i|z_k)$ when \mathcal{M} consists of the $k - \epsilon$, $k - \omega$, and SA models^a

Scenario	$k - \epsilon$	$k - \omega$	SA
S_1	1.04824e-02	6.76163e-03	9.82756e-01
S_2	5.15244e-02	8.73518e-02	8.61124e-01
S_3	4.11104e-01	5.88478e-01	4.18024e-04
S_4	7.15142e-02	4.21388e-02	8.86347e-01
S_5	9.73137e-01	2.57038e-02	1.15898e-03
S_6	1.04312e-01	1.26575e-03	8.94423e-01
S_7	1.00000e+00	1.94074e-10	2.35604e-08
S_8	9.99999e-01	9.14473e-07	1.98968e-11
S_9	9.98710e-01	1.29035e-03	2.34332e-21
S_{10}	1.00000e+00	0.00000e+00	4.95032e-13
S_{11}	3.78159e-01	6.21680e-01	1.61533e-04
S_{12}	9.42438e-01	5.36331e-02	3.92870e-03
S_{13}	0.00000e+00	3.69311e-01	6.30689e-01
S_{14}	0.00000e+00	9.74174e-01	2.58255e-02

^aIdentification numbers are taken from the source [34]. We used a uniform prior $p(M_i)$.

Acknowledgment

This research was partially supported by the European Union's Seventh Framework Programme (2007-2013) under grant agreement 605036, the Uncertainty Management for Robust Industrial Design in Aeronautics project, and by the French Agence Nationale de la Recherche under grant agreement 11-MONU-0008.

Table A6 Flow descriptions of training database

Scenario	Identification	Type ^a	Description
S_1	1400	Zero	Equilibrium boundary layer at constant pressure
S_2	1300	Fav	Near-equilibrium boundary layer in moderate negative pressure gradient
S_3	2700	Fav	Equilibrium boundary layer in mild negative pressure gradient
S_4	6300	Fav	Near-equilibrium boundary layer growing beneath potential flow on model spillway
S_5	1100	Mild adv	Boundary layer in diverging channel
S_6	2100	Diverse	Boundary layer on large airfoil-like body; pressure gradient mildly negative
S_7	2500	Mild adv	Equilibrium boundary layer in mild positive pressure gradient
S_8	2400	Diverse	Initial equilibrium boundary layer in moderate positive pressure gradient; pressure gradient abruptly decreases to zero, and flow relaxes to new equilibrium
S_9	3300	Mod adv	Boundary layer, initially at constant pressure, developing into equilibrium flow in moderate (mod) positive pressure gradient
S_{10}	0141	Str adv	Boundary layer with strong adverse pressure gradient; source [43]
S_{11}	1200	Str adv	Boundary layer in diverging channel with eventual separation
S_{12}	4400	Str adv	Boundary layer in strong positive pressure gradient
S_{13}	2133	Str adv	Boundary layer on large airfoil-like body; pressure gradient strongly positive
S_{14}	2134	Str adv	Boundary layer on large airfoil-like body; pressure gradient strongly positive, close to separation

^aThis column describes the pressure gradient, which ranges from favorable (fav) to strongly (str) adverse (adv).

References

- [1] Wilcox, D. C., *Turbulence Modeling for CFD*, DCW Industries, La Cañada, CA, 2006, pp. 53–373, Chaps. 3–6.
- [2] Cheung, S. H., Oliver, T. A., Prudencio, E. E., Prudhomme, S., and Moser, R. D., "Bayesian Uncertainty Analysis with Applications to Turbulence Modeling," *Reliability Engineering and System Safety*, Vol. 96, No. 9, 2011, pp. 1137–1149. doi:10.1016/j.res.2010.09.013
- [3] Guillas, S., Glover, N., and Malki-Epshtein, L., "Bayesian Calibration of the Constants of the $k-\epsilon$ Turbulence Model for a CFD Model of Street Canyon Flow," *Computer Methods in Applied Mechanics and Engineering*, Vol. 279, Sept. 2014, pp. 536–553. doi:10.1016/j.cma.2014.06.008
- [4] Kato, H., and Obayashi, S., "Approach for Uncertainty of Turbulence Modeling Based on Data Assimilation Technique," *Computers and Fluids*, Vol. 85, Oct. 2013, pp. 2–7. doi:10.1016/j.compfluid.2012.09.002
- [5] Edeling, W., Cinnella, P., Dwight, R., and Bijl, H., "Bayesian Estimates of Parameter Variability in the $k-\epsilon$ Turbulence Model," *Journal of Computational Physics*, Vol. 258, Feb. 2014, pp. 73–94. doi:10.1016/j.jcp.2013.10.027
- [6] Launder, B., and Sharma, B., "Application of the Energy-Dissipation Model of Turbulence to the Calculation of Flow Near a Spinning Disc," *Letters in Heat and Mass Transfer*, Vol. 1, No. 2, 1974, pp. 131–137. doi:10.1016/0094-4548(74)90150-7
- [7] Zhang, Z., Zhang, W., Zhai, Z., and Chen, Q., "Evaluation of Various Turbulence Models in Predicting Airflow and Turbulence in Enclosed Environments by CFD: Part 2 Comparison with Experimental Data from Literature," *HVAC&R Research*, Vol. 13, No. 6, 2007, pp. 871–886. doi:10.1080/10789669.2007.10391460
- [8] Harrison, K., and Bogard, D., "Comparison of RANS Turbulence Models for Prediction of Film Cooling Performance," *ASME Turbo Expo 2008: Power for Land, Sea, and Air*, American Soc. of Mechanical Engineers, Fairfield, NJ, 2008, pp. 1187–1196.

- [9] Dow, E., and Wang, Q., "Quantification of Structural Uncertainties in the $k - \omega$ Turbulence Model," AIAA Paper 2011-1762, 2011.
- [10] Kennedy, M., and O'Hagan, A., "Bayesian Calibration of Computer Models," *Journal of the Royal Statistical Society: Series B (Statistical Methodology)*, Vol. 63, No. 3, 2001, pp. 425–464. doi:10.1111/1467-9868.00294
- [11] Singh, A., and Duraisamy, K., "Using Field Inversion to Quantify Functional Errors in Turbulence Closures," *Physics of Fluids*, Vol. 28, No. 4, 2016, Paper 045110. doi:10.1063/1.4947045
- [12] Xiao, H., Wu, J., Wang, J., Sun, R., and Roy, C., "Quantifying and Reducing Model-Form Uncertainties in Reynolds-Averaged Navier–Stokes Simulations: A Data-Driven, Physics-Informed Bayesian Approach," *Journal of Computational Physics*, Vol. 324, Nov. 2016, pp. 115–136. doi:10.1016/j.jcp.2016.07.038
- [13] Poroseva, S., Colmenares, J., and Murman, S., "RANS Simulations of a Channel Flow with a New Velocity/Pressure-Gradient Model," AIAA Paper 2015-3067, 2015.
- [14] Poroseva, S., Colmenares, F. J. D., and Murman, S., "On the Accuracy of RANS Simulations with DNS Data," *Physics of Fluids*, Vol. 28, No. 11, 2016, Paper 115102. doi:10.1063/1.4966639
- [15] Poroseva, S. V., Hussaini, M. Y., and Woodruff, S. L., "Improving the Predictive Capability of Turbulence Models Using Evidence Theory," *AIAA Journal*, Vol. 44, No. 6, 2006, pp. 1220–1228. doi:10.2514/1.15756
- [16] Poroseva, S., Lay, N., and Hussaini, M., "Multimodel Approach Based on Evidence Theory for Forecasting Hurricane/Typhoon Tracks: Further Improvements," *Monthly Weather Review*, Vol. 138, No. 2, 2010, pp. 405–420. doi:10.1175/2009MWR2733.1
- [17] Diomede, T., Davolio, S., Marsigli, C., Miglietta, M., Moscatello, A., Papetti, P., and Paccagnella, T. E. A., "Discharge Prediction Based on Multi-Model Precipitation Forecasts," *Meteorology and Atmospheric Physics*, Vol. 101, No. 3, 2008, pp. 245–265. doi:10.1007/s00703-007-0285-0
- [18] Duan, Q., Ajami, N., Gao, X., and Sorooshian, S., "Multi-Model Ensemble Hydrologic Prediction Using Bayesian Model Averaging," *Advances in Water Resources*, Vol. 30, No. 5, 2007, pp. 1371–1386. doi:10.1016/j.advwatres.2006.11.014
- [19] Tebaldi, C., and Knutti, R., "The Use of the Multi-Model Ensemble in Probabilistic Climate Projections," *Philosophical Transactions of the Royal Society of London, Series A: Mathematical, Physical and Engineering Sciences*, Vol. 365, No. 1857, 2007, pp. 2053–2075. doi:10.1098/rsta.2007.2076
- [20] Draper, D., "Assessment and Propagation of Model Uncertainty," *Journal of the Royal Statistical Society: Series B (Methodological)*, Vol. 57, No. 1, 1995, pp. 45–97.
- [21] Rojas, R., Kahunde, S., Peeters, L., Batelaan, O., Feyen, L., and Dassargues, A., "Application of a Multimodel Approach to Account for Conceptual Model and Scenario Uncertainties in Groundwater Modelling," *Journal of Hydrology*, Vol. 394, No. 3, 2010, pp. 416–435. doi:10.1016/j.jhydrol.2010.09.016
- [22] Hoeting, J., Madigan, D., Raftery, A., and Volinsky, C., "Bayesian Model Averaging: A Tutorial," *Statistical Science*, Vol. 14, No. 4, 1999, pp. 382–401.
- [23] Edeling, W., Cinnella, P., and Dwight, R., "Predictive RANS Simulations via Bayesian Model-Scenario Averaging," *Journal of Computational Physics*, Vol. 275, Oct. 2014, pp. 65–91. doi:10.1016/j.jcp.2014.06.052
- [24] Oliver, T., and Moser, R., "Bayesian Uncertainty Quantification Applied to RANS Turbulence Models," *Journal of Physics: Conference Series*, Vol. 318, No. 4, 2011, Paper 042032.
- [25] Margheri, L., Meldi, M., Salvetti, M., and Sagaut, P., "Epistemic Uncertainties in RANS Model Free Coefficients," *Computers and Fluids*, Vol. 102, Oct. 2014, pp. 315–335. doi:10.1016/j.compfluid.2014.06.029
- [26] Papadimitriou, D., and Papadimitriou, C., "Bayesian Uncertainty Quantification of Turbulence Models Based on High-Order Adjoint," *Computers and Fluids*, Vol. 120, Oct. 2015, pp. 82–97. doi:10.1016/j.compfluid.2015.07.019
- [27] Hastings, W. K., "Monte Carlo Sampling Methods Using Markov Chains and their Applications," *Biometrika*, Vol. 57, No. 1, 1970, pp. 97–109. doi:10.1093/biomet/57.1.97
- [28] Eldred, M., and Burkardt, J., "Comparison of Non-Intrusive Polynomial Chaos and Stochastic Collocation Methods for Uncertainty Quantification," AIAA Paper 2009-0976, 2009, pp. 1–20.
- [29] Cheung, S., and Beck, J., "Calculation of Posterior Probabilities for Bayesian Model Class Assessment and Averaging from Posterior Samples Based on Dynamic System Data," *Computer-Aided Civil and Infrastructure Engineering*, Vol. 25, No. 5, 2010, pp. 304–321. doi:10.1111/mice.2010.25.issue-5
- [30] Edeling, W. N., Cinnella, P., and Dwight, R., "MCMC Traces of Posterior Distributions of Closure Coefficients for 6 Turbulence Models," 2016, www.researchgate.net/publication/308609583_MCMC_traces_of_posterior_distributions_of_closure_coefficients_for_6_turbulence_models_ASCII_format [retrieved 25 Sept. 2016].
- [31] Beck, J., "Bayesian System Identification Based on Probability Logic," *Structural Control and Health Monitoring*, Vol. 17, No. 7, 2010, pp. 825–847. doi:10.1002/stc.v17:7
- [32] Chib, S., and Jeliazkov, I., "Marginal Likelihood from the Metropolis–Hastings Output," *Journal of the American Statistical Association*, Vol. 96, No. 453, 2001, pp. 270–281. doi:10.1198/016214501750332848
- [33] Edeling, W., Dwight, R., and Cinnella, P., "Simplex-Stochastic Collocation Method with Improved Scalability," *Journal of Computational Physics*, Vol. 310, April 2016, pp. 301–328. doi:10.1016/j.jcp.2015.12.034
- [34] Coles, D., and Hirst, E., "Computation of Turbulent Boundary Layers," *Proceedings of AFOSR-IFP Stanford Conference*, Vol. 2, Thermosciences Div., Stanford Univ., Stanford, CA, 1968.
- [35] Greenshields, C. J., "OpenFOAM User Guide," *OpenFOAM Foundation Ltd, Version*, Vol. 3, No. 1, 2015.
- [36] Breuer, M., Peller, N., Rapp, C., and Manhart, M., "Flow over Periodic Hills—Numerical and Experimental Study in a Wide Range of Reynolds Numbers," *Computers and Fluids*, Vol. 38, No. 2, 2009, pp. 433–457. doi:10.1016/j.compfluid.2008.05.002
- [37] Kuzmin, A., "On the Lambda-Shock Formation on ONERA M6 Wing," *International Journal of Applied Engineering Research*, Vol. 9, No. 20, 2014, pp. 7029–7038.
- [38] Schmitt, V., and Charpin, F., "Pressure Distributions on the ONERA-M6-Wing at Transonic Mach Numbers," *Experimental Data Base for Computer Program Assessment*, Vol. 4, Rept. of the Fluid Dynamics Panel Working Group 04, AGARD AR 138, May 1979.
- [39] Lerat, A., Cinnella, P., Michel, B., and Falissard, F., "High-Order Residual-Based Compact Schemes for Aerodynamics and Aeroacoustics," *Computers and Fluids*, Vol. 61, May 2012, pp. 31–38. doi:10.1016/j.compfluid.2011.07.017
- [40] Huang, Y., Cinnella, P., and Lerat, A., "A Third-Order Accurate Centered Scheme for Turbulent Compressible Flow Calculations in Aerodynamics," *Numerical Methods for Fluid Dynamics*, Vol. 6, 1998, pp. 355–361.
- [41] "ONERA M6 Wing," *NPARC Alliance Validation Archive* [online database], NASA, 2017, <https://www.grc.nasa.gov/www/wind/valid/m6wing/m6wing.html> [retrieved 2 Oct. 2017].
- [42] *FLUENT–3-D Transonic Flow over a Wing* [online database], Cornell Univ., Ithaca, NY, 2017 <https://confluence.cornell.edu/display/SIMULATION/FLUENT+-+3-D+Transonic+Flow+Over+a+Wing> [retrieved 9 Oct. 2017].
- [43] Kline, S., "Proceedings of the 1980–1981 AFOSR-HTTM-Stanford Conference on Complex Turbulent Flows: Comparison of Computation and Experiment," *Objectives, Evaluation of Data, Specifications of Test Cases, Discussion and Position Papers*, Vol. 1, Thermosciences Div., Stanford Univ., Stanford, CA, 1981.

C. Pettit
Associate Editor